Ultrasound attenuation measurement in the presence of scatterer variation for reduction of shadowing and enhancement

G.M. Treece, R.W. Prager and A.H. Gee

CUED/F-INFENG/TR 502

November 2004

Cambridge University Engineering Department
Trumpington Street
Cambridge CB2 1PZ
England

Corresponding e-mail: gmt11@eng.cam.ac.uk

Abstract

Pulse-echo ultrasound display relies on many assumptions which are known to be incorrect. Departure from these makes interpretation of conventional ultrasound images difficult, and 3D visualisations harder still. For instance, sound attenuation is not simply a function of depth, and this leads to shadowing and enhancement. Attempts to reduce such artefacts by estimating attenuation locally have been frustrated by large statistical variations and the influence of scatterer type. Hence estimates are not of sufficiently high resolution or are only applicable in well specified scatterer distributions. In this paper we examine the mathematical framework for attenuation measurement from pulse-echo ultrasound, concentrating on the effect of the type of scatterer on existing techniques, and propose a less scatterer-sensitive alternative. We also present novel techniques for handling the large statistical fluctuations, based on combined assumptions of monotonicity and smoothness. Shadowing and enhancement correction algorithms are tested on *in vitro* data, using a real time 3D RF ultrasound acquisition system developed for this purpose. The *in vitro* results support the analysis of scatterer type sensitivity, and this leads to visible differences in attenuation estimates from each technique. Nevertheless, it *is* possible to reduce the statistical variations sufficiently to allow the correction of shadowing and enhancement.

Contents

1 Introduction

It is well known that medical ultrasound images contain many artefacts due to the complex nature of sound transmission and reflection in anatomical structures. One such group of artefacts is due to the varying attenuation of sound in the medium. We typically only display the magnitude of the reflected signal at the transducer over time, which can be interpreted as depth assuming a constant speed of sound. However, this is affected by the attenuation properties of the tissue above as well as the backscatter (reflection) at the indicated depth. Reduction in signal amplitude is typically compensated by providing a manual estimate of the attenuation, in the form of a time-gain-compensation (TGC) curve. In practice, a set of gain sliders corresponding to different tissue depths are moved until a given image looks relatively homogeneous.

The assumption underlying TGC, that the attenuation is uniform across the image at a given depth, is frequently violated. Ultrasound images show dark regions (shadowing) below highly attenuating tissue which has been under-compensated, and light regions (enhancement) below less attenuating tissue which has been over-compensated. So long as their origin is understood, shadowing and enhancement are not altogether a bad thing — in effect they are indicators of the relative attenuation of tissue (something which is otherwise not displayed). These can in some cases have clinical significance, for instance in detecting liver disease (Bevan and Sherar, 2001) or certain tumours (Tu et al., 2003), or even for monitoring temperature change (Tyréus and Diederich, 2004).

Nevertheless, there are several motivating factors for removing such artefacts. Firstly, they complicate the interpretation of ultrasound images. Even if attenuation is clinically significant, would it not be better to display material backscatter and attenuation properties separately, rather than having to infer them from inconsistencies in the image? In addition, the ability to infer attenuation from ultrasound images is reliant on the traditional B-scan visualisation: as 3D ultrasound gains in popularity, so does the ability to view US data in different ways, making such artefacts much harder to spot. Secondly, images containing artefacts make downstream processing (for instance registration or segmentation) much harder. Images of backscatter and attenuation which are more representative of actual tissue properties are likely to be easier to handle and at the same time provide additional information for such algorithms.

1.1 Reduction of shadowing and enhancement

Approaches to the reduction of ultrasound shadowing and enhancement can be loosely split into those which directly aim to make images more homogeneous, and those whose aim is to provide quantitative data by separate measurement of backscatter and attenuation coefficients. There have also been attempts to *detect* rather than reduce shadows (Drukker et al., 2003), although in this case it was really signal dropout rather than shadowing *per se* that was being detected. In the homogeneous approach, for instance by Xiao et al. (2002), the image is first classified into different tissue types before imposing uniform gain within each class. Such approaches are clearly dependent on a certain level of natural homogeneity in the data, and have the potential to falsely 'correct' shadows or enhancements where this assumption does not hold.

O'Donnel and H. F. Reilly (1985) and Bridal et al. (2000) employ an alternative approach which also relies on classification. If a region in the image is known to be from tissue with the same properties, and time gain compensation has not been used (or has been calibrated for), then the attenuation can be estimated directly from the slope of the log amplitude with depth. If this can be measured with sufficient locality, the original ultrasound image can be corrected for the known attenuation, resulting in a *quantitative* backscatter image. However, as in the previous methods, such techniques are hampered by the necessity to have sufficiently homogeneous regions for the classification to be successful, and are based on assumptions which are not necessarily true for real images. Similar approaches are employed by Walach et al. (1989); Valckx et al. (2000); Knipp et al. (1997).

Rather than assuming homogeneity in the images, Hughes and Duck (1997) make the less constraining assumption that the attenuation at any given point is linearly related to the magnitude of backscatter. Under this assumption, the image can be compensated by appropriate integration of the received sound amplitude. Although there are situations where this relationship is not valid (in particular for certain kinds of tumours), it is evident from images successfully corrected by this technique that the assumptions hold in many cases. Clearly the method is not capable of providing an independent attenuation image.

However, there is an alternative independent way to measure attenuation. Conventional ultrasound images are visualisations of the amplitude of the sound received back at the transducer from a high frequency focused pulse transmitted into the medium. Under certain conditions, it is possible to estimate the attenuation by looking at the spectrum of the radio-frequency (RF) ultrasound, rather than simply the amplitude, and it is on this that the remainder of this paper will concentrate. There has already been significant work in this area, much of which was reported some twenty years ago. It is therefore prudent to start by reviewing some of the main issues which have limited the development and application of these techniques.

1.2 Estimation of attenuation from backscattered spectra

One of the difficulties in using the RF spectrum to estimate attenuation is the trade off in frequency and time resolution implied in using short-time Fourier transforms (Fink et al., 1983; Flax et al., 1983). This has led to the investigation of auto-regressive techniques for measuring model parameters, for instance centre frequency, with better resolution than the conventional Fourier approach, at least in simulation (Baldeweck et al., 1995; Girault et al., 1998). In practice, however, it is not the resolution with which the spectrum can be measured which is the limiting factor, but the characteristics of the signal itself. Fully developed ultrasound backscatter follows a Rayleigh distribution (Prager et al., 2003) which is characterised by large variations in both phase and amplitude about a mean value. Typically it is necessary to use a considerable number of data points to give a good estimate of the mean. The spectra of such signals show a similar distribution. This statistical variation is generally much larger than the small changes which we need to measure to estimate attenuation.

A second difficulty is due to the conditions under which attenuation can be estimated from spectral properties: namely that diffraction and refraction can be ignored, and the scatterer type (and hence the frequency dependence of backscatter) is constant throughout the sample. Although the latter of these restrictions *does* allow for variation in the *magnitude* of backscatter, in practice the frequency dependence changes with different tissue types, and this tends to be a more limiting assumption than the former. Hence much of the work on attenuation estimation has been demonstrated on simulated data, or phantoms where the backscatter properties are closely controlled (Knipp et al., 1997). Attempts have been made to correct for overlying layers with different characteristics (thus modelling the effect of skin) (Lu et al., 1995) or to spot discontinuities in the received spectra (thus detecting boundaries of tissue with varying scatterer types) (Gorce et al., 2002).

It should be noted that all of the above techniques are designed to detect attenuation from pulse-echo ultrasound systems, i.e. from backscattered signals. If the aim is to measure attenuation directly, rather than correct conventional images, there is an alternative *through transmission* technique which uses a separate receiver at the opposite side of the sample from the transmitting transducer. Clearly this physical layout limits the application of the technique, but, in the right application, it can generate much better attenuation estimates than from pulse-echo systems (Damilakis et al., 2002).

The primary aims of this paper are to investigate the effect of scatterer type on the estimation of attenuation, and also to investigate ways of efficiently handling the large statistical fluctuations that are present in such estimates. The hope is that this will increase the locality and applicability of attenuation measurement, and hopefully enable its use in calculating backscatter images in real pulse-echo ultrasound data.

We will start in Section 2 by re-examining two existing techniques based on centre frequency and the slope of the calibrated spectra, noting the effect of scatterer type on each technique and extending the latter to cope with differences. Then we will show how such techniques can be used to correct the conventional ultrasound B-scan. In Section 3 we will outline a new technique for coping with the statistical variations in spectral estimates of attenuation. We will also describe the real time 3D RF acquisition system we have developed to allow us to acquire the necessary ultrasound data. Finally Section 4 contains the results of applying this technique on different test objects.

2 Analysis of attenuation and backscatter in pulse-echo systems

Before analysing the effects of attenuation and backscatter, we need a model for the pulse-echo ultrasound system. Firstly we simplify the system by ignoring the effects of diffraction and refraction, and make the usual assumption that the backscatter is only a very small percentage of the transmitted sound (i.e. the Born approximation). Under these assumptions, the backscattered signal, S, received at the ultrasound probe held in a particular position over a particular sample, is a function of location x, y and frequency f. This can be represented by:

$$S(x, y, f) = P(x, y, f)A(x, y, f)B(x, y, f) \tag{1}$$

where $P(x, y, f)$ describes the transmitted pulse, and is dependent only on the probe design and settings, $A(x, y, f)$ describes the cumulative attenuation of the sample, and $B(x, y, f)$ the backscatter of the sample. In essence, the Born approximation allows us to model the system as a simple multiplication (in the frequency domain) of the pulse and backscatter characteristics. Ignoring diffraction and refraction allows us to assume that P is independent of the sample being scanned.

According to Nicholas et al. (1982), the backscatter can be modelled as a power of f:

$$B(x, y, f) = B_0(x, y)f^z \tag{2}$$

where z varies from 0 for specular reflection to 4 for Rayleigh scattering, and is typically in the range 1 to 2 for human tissue.

For most tissues (but *not* for ultrasound contrast agents (Chen et al., 2002)), we can additionally assume that the attenuation in Neper is linearly proportional to frequency (Flax et al., 1983), hence:

$$A(x, y, f) = e^{-\alpha(x,y)f} \tag{3}$$

where $\alpha(x, y)$ is the total cumulative round trip attenuation in the sample from the probe face to depth y. For homogeneous samples, $\frac{\alpha}{2y}$ is generally quoted in Neper/MHz/cm, and is typically in the range 0.3 to 0.7 in human tissue.

2.1 Attenuation from measurement of centre frequency

If we make the assumption that the pulse generated by the probe is approximately Gaussian, with centre frequency f_0 and variance σ^2, then:

$$P(x, y, f) = P_0(x, y) e^{\frac{-[f - f_0(x,y)]^2}{2\sigma(x,y)^2}} \tag{4}$$

Putting eqs. (2) to (4) in eq. (1) gives:

$$S(x, y, f) = P_0(x, y) B_0(x, y) e^{\frac{-[f - f_0(x,y)]^2}{2\sigma(x,y)^2}} e^{-\alpha(x,y) f} f^z \tag{5}$$

i.e. at a particular location, x, y:

$$\begin{aligned} S(f) &= P_0 B_0 e^{\frac{-(f-f_0)^2}{2\sigma^2}} e^{-\alpha f} f^z && (6) \\ &= P_0 B_0 e^{-\alpha\left(f_0 - \frac{\alpha\sigma^2}{2}\right)} e^{\frac{-\left[f-(f_0-\alpha\sigma^2)\right]^2}{2\sigma^2}} f^z && (7) \\ &\propto e^{\frac{-\left[f-(f_0-\alpha\sigma^2)\right]^2}{2\sigma^2}} f^z && (8) \end{aligned}$$

It can be seen that the attenuation effectively reduces the centre frequency of the received signal by $\alpha\sigma^2$. Following Flax et al. (1983), in order to analyze the effect of the backscatter term, it is convenient to express f^z as an exponential, noting that since we are only interested in proportionality, we can drop any scaling factors which are not functions of frequency, f:

$$\begin{aligned} f^z = e^{z \ln(f)} &= e^{\left[z \ln f_0 + z \ln\left(1 + \frac{f-f_0}{f_0}\right)\right]} \\ &\approx {f_0}^z e^{z\left[\frac{f-f_0}{f_0} - \frac{(f-f_0)^2}{2{f_0}^2} + O\left(\frac{(f-f_0)^3}{f_0^3}\right)\right]} \\ &\propto e^{\frac{z}{{f_0}^2}\left[2 f f_0 - \frac{f^2}{2}\right]} && (9) \end{aligned}$$

Combining eq. (9) with eq. (8) leads to:

$$S(f) \propto e^{\left\{-\frac{{f_0}^2 + z\sigma^2}{2\sigma^2 {f_0}^2}\left[f^2 - \frac{2f_0\left({f_0}^2 - \alpha\sigma^2 f_0 + 2z\sigma^2\right)}{{f_0}^2 + z\sigma^2} f\right]\right\}} \tag{10}$$

which in turn implies that:

$$S(f) \propto e^{\frac{-\left(f - f_0'\right)^2}{2\sigma'^2}} \tag{11}$$

where:

$$\begin{aligned} \sigma'^2 &= \sigma^2 \frac{{f_0}^2}{{f_0}^2 + z\sigma^2} && (12) \\ f_0' &= \frac{f_0\left({f_0}^2 - \alpha\sigma^2 f_0 + 2z\sigma^2\right)}{{f_0}^2 + z\sigma^2} \\ &= f_0 - \alpha\sigma^2\left(\frac{{f_0}^2}{{f_0}^2 + z\sigma^2}\right) + \frac{z\sigma^2}{f_0}\left(\frac{{f_0}^2}{{f_0}^2 + z\sigma^2}\right) \\ &= f_0 - \alpha\sigma'^2 + \frac{z\sigma'^2}{f_0} && (13) \end{aligned}$$

Hence the attenuation α *reduces* the centre frequency ${f_0}'$ of the received response, and the scatter power z *increases* the centre frequency and *reduces* the bandwidth σ'. Note that eq. (13) is *not* the same as was given by Flax et al. (1983)[1].

We can therefore calculate an estimate of the attenuation α_e at a point x, y by comparing the centre frequency of the response from the sample with that from a non-attenuating uniform phantom. It is not practical to obtain an estimate of bandwidth σ' from the sample itself, hence we use σ, the transducer bandwidth[2]. Denoting phantom measurements with a subscript p, we have:

$$\begin{aligned}
\alpha_e &= \frac{{f_0}'_p - {f_0}'}{\sigma^2} && (14)\\
&= \alpha\frac{\sigma'^2}{\sigma^2} + \frac{z_p\frac{\sigma'^2_p}{\sigma^2} - z\frac{\sigma'^2}{\sigma^2}}{f_0} + O\left(\frac{(f_0-f)^3}{f_0^3}\right) \\
&\approx \alpha + \frac{z_p - z}{f_0} + O\left(\frac{z\sigma^2}{f_0^2}\right) + O\left(\frac{(f_0-f)^3}{f_0^3}\right) && (15)
\end{aligned}$$

Note that if the phantom contains scatterers which are nearly Rayleigh ($z_p \approx 4$), then $\sigma'_p < \sigma' < \sigma$, and in all likelihood $z < z_p$, which results in the second term partially compensating for reduction in value of the first term due to the change in bandwidth. This means that the attenuation estimate is likely to be somewhat better than is implied by the simplified equation.

2.2 Attenuation from spectral division

An alternative, which does not require the assumption of eq. (4) that the pulse is Gaussian, is to divide the sample spectrum, S, by one from a non-attenuating uniform phantom, S_p, in which case:

$$\frac{S(x,y,f)}{S_p(x,y,f)} = \frac{A(x,y,f)B(x,y,f)}{A_p(x,y,f)B_p(x,y,f)} \qquad (16)$$

since we have already stated that $P(x, y, f)$ is independent of the sample being scanned.

Combining with eq (3) and (2), and taking the natural logarithm, gives (at a particular location x, y):

$$\begin{aligned}
\ln\left(\frac{S(f)}{S_p(f)}\right) &= \ln\left(\frac{B_0}{B_{0p}}\right) - \alpha f + (z - z_p)\ln f && (17)\\
&= a + bf + c\ln f && (18)
\end{aligned}$$

If we ignore differences in the frequency dependence of backscatter z between the phantom and the sample, then the attenuation is given simply by the negative of the slope of this function in frequency, b. This can be found by linear regression of $a_0 + b_0 f$, and is the method employed by Knipp et al. (1997). If s are the measured data (i.e. the log of the measured spectrum divided by the calibration spectrum at location x, y) at frequencies f, then the least-squares solution is:

$$\begin{aligned}
b_0 &= \frac{k_1}{k_0} \\
a_0 &= \frac{\sum s - b_0 \sum f}{\sum 1} && (19)
\end{aligned}$$

[1]Equation (30) in (Flax et al., 1983) is not a valid simplification of equation (29).
[2]Another possibility would be to use the measured bandwidth from the phantom, σ'_p.

where

$$\begin{aligned} k_0 &= \sum f^2 - \frac{\left(\sum f\right)^2}{\sum 1} \\ k_1 &= \sum fs - \frac{\sum f \sum s}{\sum 1} \end{aligned} \tag{20}$$

and all the summations are taken over all the available data points, i.e. all frequencies within the bandwidth of the ultrasound signal.

We now extend the analysis to see how real differences in backscatter over frequency affect this measurement, by evaluating b_0 using eq. (19), with s described by eq. (17). This leads to an error in b_0 (and hence attenuation estimation):

$$\alpha_e = \alpha + (z_p - z)\frac{\sum f \ln f - \frac{\sum f \sum \ln f}{\sum 1}}{\sum f^2 - \frac{\left(\sum f\right)^2}{\sum 1}} \tag{21}$$

We can estimate this error by taking the summations to be over a range $(f_0 - f_b)\ldots(f_0 + f_b)$, where f_0 is the centre frequency, and f_b is half the bandwidth of the pulse. In the limit as df tends to zero, then:

$$\begin{aligned} \sum 1 = \int_{f_0-f_b}^{f_0+f_b} 1 &= 2f_b \\ \sum f = \int_{f_0-f_b}^{f_0+f_b} f &= 2f_0 f_b \\ \sum f^2 = \int_{f_0-f_b}^{f_0+f_b} f^2 &= 2f_0^2 f_b + \frac{2}{3} f_b^3 \\ \sum \ln f = \int_{f_0-f_b}^{f_0+f_b} \ln f &= -2f_b + f_0 \ln\left(\frac{f_0+f_b}{f_0-f_b}\right) + f_b \ln\left[(f_0+f_b)(f_0-f_b)\right] \\ \sum f \ln f = \int_{f_0-f_b}^{f_0+f_b} f \ln f &= -f_0 f_b + \frac{1}{2}\left(f_0^2 + f_b^2\right) \ln\left(\frac{f_0+f_b}{f_0-f_b}\right) + f_0 f_b \ln\left[(f_0+f_b)(f_0-f_b)\right] \end{aligned}$$

Hence, if the fractional bandwidth, $\lambda = \frac{f_b}{f_0}$:

$$\begin{aligned} \alpha_e &= \alpha + (z_p - z)\frac{6\lambda + 3(\lambda^2 - 1)\ln\left(\frac{1+\lambda}{1-\lambda}\right)}{4 f_0 \lambda^3} \\ \alpha_e &= \alpha + \frac{(z_p - z)}{f_0} + O\left(\lambda^5\right) \end{aligned} \tag{22}$$

Eq. (22) reduces to eq. (15) in the limit, i.e. the effect of actual differences in backscatter is similar in both cases. However, eq. (22) is far more precise, and in practice, the centre frequency estimate is less affected by differences in backscatter.

2.3 Attenuation and backscatter power from spectral division

Equation (17) demonstrates that the attenuation α and backscatter power z are not linearly related, and hence can be found simultaneously by regression of $a_1 + b_1 f + c_1 \ln f$ to the spectrally divided data s as in the previous section. This leads to a new technique in which the coefficients b_1 and c_1, which are estimates of $(-\alpha)$ and $(z - z_p)$ respectively, can be found from:

$$\begin{aligned} c_1 &= \frac{k_0 k_4 - k_1 k_3}{k_0 k_2 - {k_3}^2} \\ b_1 &= \frac{k_1 - k_3 c_1}{k_0} \\ a_1 &= \frac{\sum s - b_1 \sum f - c_1 \sum \ln f}{\sum 1} \end{aligned} \tag{23}$$

where k_0 and k_1 are defined in eq. (20), and:

$$\begin{aligned} k_2 &= \sum (\ln f)^2 - \frac{(\sum \ln f)^2}{\sum 1} \\ k_3 &= \sum f \ln f - \frac{\sum f \sum \ln f}{\sum 1} \\ k_4 &= \sum s \ln f - \frac{\sum s \sum \ln f}{\sum 1} \end{aligned} \tag{24}$$

This new technique potentially allows the estimation of attenuation in tissues which have different scatterer types.

2.4 Using attenuation to provide a backscatter image

The motivation for estimating the attenuation in the sample is to provide an image which has uniform gain for regions with uniform backscatter properties, i.e. $B(x, y, f)$. Ultrasound B-scans are images of the amplitude of the sound received at the transducer, integrated across all frequencies within the bandwidth of the probe, $S_I(x, y)$. We therefore require an estimate of $B_I(x, y)$, the *integrated backscatter* of the sample:

$$B_I(x, y) = \int_{f_0 - f_b}^{f_0 + f_b} \frac{S(x, y, f)}{P(x, y, f) A(x, y, f)} \tag{25}$$

In practice, we need to use short-time Fourier transforms to calculate the frequency dependence of S. This process, followed by integration across frequency, generates a backscatter image which has very different noise characteristics than a conventional B-scan[3]. Ideally, we would like to preserve the original B-scan in every respect other than to correct the gain, since the particular patterns of speckle can themselves be clinically useful. We have already seen in eq. (12) that, if we assume the pulse is Gaussian, the bandwidth is not affected by attenuation, and only slightly modified by changes in the frequency dependence of backscatter. If we ignore these changes to bandwidth, and note that shifts in the centre frequency will have no effect on the integrated backscatter, then, using eq. (7):

$$B_I(x, y) \approx \frac{S_I(x, y)}{P_{pI}(x, y) e^{-\alpha_e(x,y)\left(f_{p0}(x,y) - \frac{\alpha_e(x,y)\sigma_p(x,y)^2}{2}\right)}} \tag{26}$$

where P_I is the gain of the probe integrated over frequency, and the subscript p denotes values measured in an appropriate phantom.

[3] This is equally true if we use the spectral division method to estimate B_0 directly.

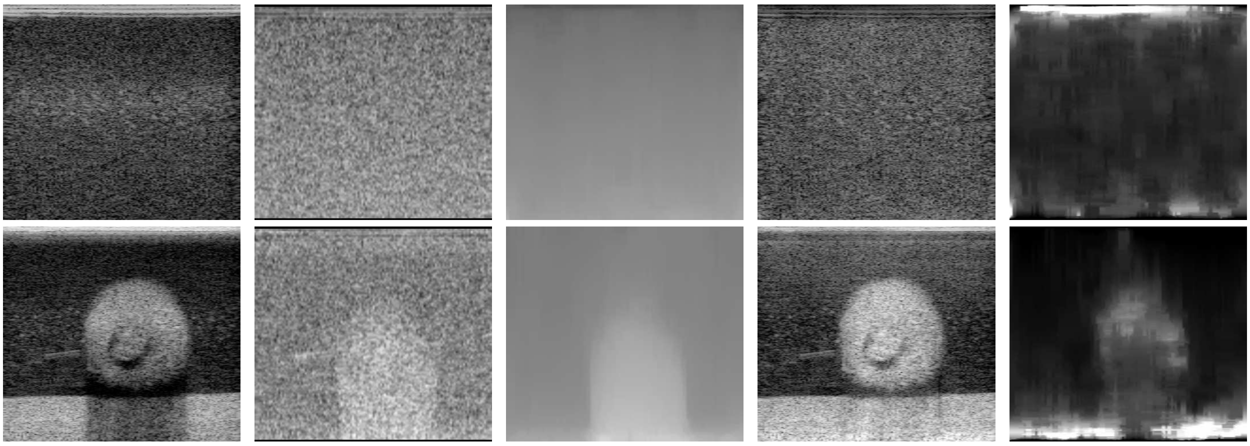

(a) (b) (c) (d) (e)

Figure 1: **Generating a backscatter image.** The top row shows data from a homogeneous calibration phantom with known attenuation, the lower row from a stuffed olive embedded in a minimally attenuating medium (jelly mixed with flour). (a) B-scans of each data set. (b) The raw estimate of cumulative attenuation. (c) Derived cumulative attenuation after enforcing monotonicity and smoothness constraints. (d) Backscatter image. (e) An estimate of the local attenuation coefficient can also be derived from (c).

Eq. (26) can be further simplified if we note that changes in f_0 and σ across the field of view of the probe will be small compared to errors in the measurement of α_e. In many probes it is also acceptable to ignore the variation of integrated gain P_I in the x (lateral) direction, in which case:

$$B_I(x,y) \approx \frac{S_I(x,y)}{P_{pI}(y) e^{-\alpha_e(x,y)\left(f_{p0} - \frac{\alpha_e(x,y)\sigma_p{}^2}{2}\right)}} \tag{27}$$

Hence in order to correct the B-scan, we need P_I, f_0 and σ, which are considered fixed for a given probe design and settings, and both the received signal S_I and attenuation estimate α_e from the sample being scanned. Figure 1 demonstrates the process, for a scan of a homogeneous phantom and an olive embedded in jelly mixed with flour. The steps in deriving the estimate of cumulative attenuation (c) from the raw data (b) are outlined in Section 3.

Figure 1(e) shows the local attenuation coefficient β_e of the sample. This can be derived from the cumulative attenuation estimate α_e:

$$\beta_e = \frac{1}{2}\frac{d\alpha_e}{dy} \tag{28}$$

where the factor of two appears since α_e is accumulated over twice the depth y. In practice α_e is a very noisy estimate, and this noise will be amplified by taking the differential. However, note that we do not need to calculate β_e if we only want to provide a corrected backscatter image, as in Figure 1(d).

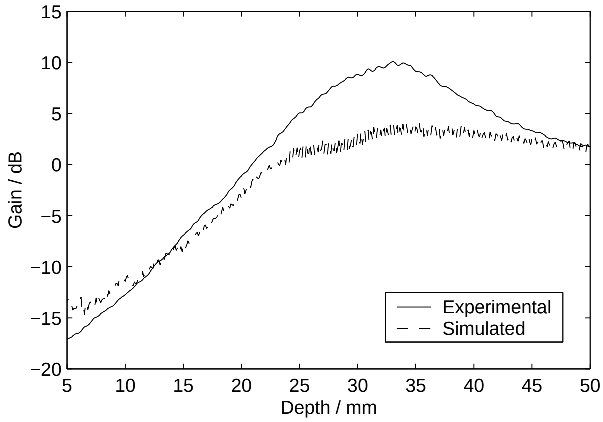

(a) Gain calibration curve

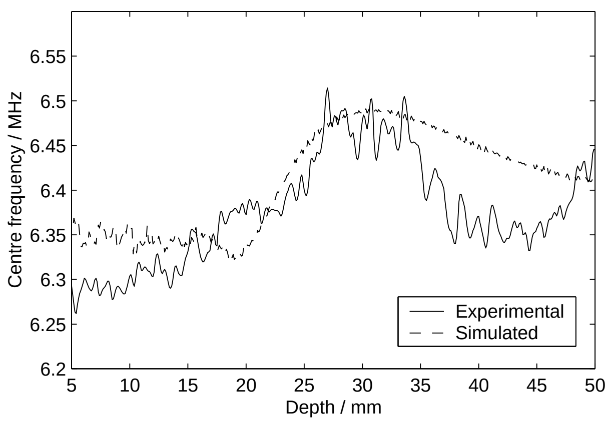

(b) Frequency calibration curve

Figure 2: **Experimental and simulated calibration curves.** A homogeneous phantom with known attenuation was scanned many times with a 5-10MHz ultrasound probe. The spectrum was averaged and corrected for attenuation at each frequency. Magnitude (a) and centre frequency (b) across the probe bandwidth were estimated from this data and compared with simulations. The probe had a tighter focus than the simple simulation predicts, but nevertheless both curves show the same form of variations in both magnitude and frequency.

3 Method

3.1 Measurement of calibrated spectra

All the techniques described in Section 2 require calibration of the ultrasound probe to calculate $S_p(x, y, f)$, from which $P_I(y)$, f_0 and σ can also be derived. This can be estimated from multiple scans of a homogeneous phantom (J. M. Kofler and Madsen, 2001). Each vector in each scan is Fourier transformed and averaged — typically 50 scans each containing 128 vectors are sufficient to give a good estimate. The same sampling and window length are used as when calculating $S(x, y, f)$ from the sample. Typically, for a 5-10MHz probe, we sample and pass-band filter the signals at 66.6MHz, then convert to baseband (using a notional centre frequency of 6.5MHz) and decimate by a factor of four. The window length is set to 12 cycles of the centre frequency, which gives a reasonable trade-off between time and frequency resolution.

S_p is first corrected for the known attenuation of the phantom, by direct application of eq. (3), thus effectively setting $\alpha_p = 0$. For the spectral division technique, the spectrum is then averaged in the x (lateral) direction, and the same resulting $S_p(y, f)$ used for each vector in eq. (17). The integrated gain $P_I(y)$, average centre frequency f_0 and bandwidth σ are calculated from this averaged spectrum, and these values used in eq. (27). Figure 2(a) shows an experimental $P_I(y)$ curve compared to a simulation using the same probe settings in Field II[4] (Jensen, 1996). Having estimated the calibration values, we simply need to know $S(x, y, f)$ for each scan which we intend to correct.

For the centre frequency technique, we need a method for determining the centre frequency in the sample $f_0{}'$ and in the calibration phantom f'_{0p} *at each depth* y. It can be seen from both the

[4] http://www.es.oersted.dtu.dk/staff/jaj/field/

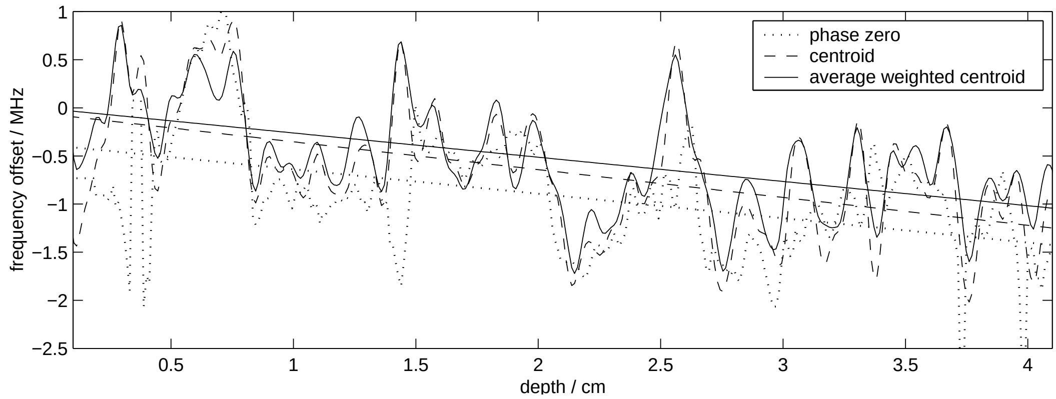

Figure 3: **Centre frequency estimation.** The graph shows several estimates of centre frequency from one vector from a scan of a homogeneous attenuating phantom, with a 5-10MHz ultrasound probe. For each estimate, both the measured frequency and a least-squares linear fit are shown. It is clear that although all the frequency estimation techniques follow a similar pattern, there is considerable difference in estimation of attenuation from each. These differences are significant even in the least-squares estimates.

experimental and simulated centre frequency estimates in Figure 2(b) that this varies slightly with depth. Whereas f_0 is only used as a scaling factor in eq. (27), and this variation can be safely ignored, in eq. (14) the expected differences between frequencies are of the same order as the variation with depth. Hence, a different value of ${f_0}'_p$ is used at each depth in eq. (14).

There are a variety of ways to measure f_0. It can be estimated from the first non-zero location at which the complex auto-correlation of the analytic RF signal has zero phase. This can be done very efficiently by slight adaptation of an algorithm used in elastography to estimate relative time shifts between similar RF signals (Pesavento et al., 1999). Alternatively we can calculate the centroid (within an appropriate bandwidth) of the local spectrum of the signal. Both of these are shown in Figure 3, for a typical RF vector from the homogeneous phantom.

It is immediately obvious from this figure that the variation of f_0 is very large, since we are estimating it from a backscattered signal with approximately Rayleigh statistics. A better way to estimate f_0 is to take the average of two centroids, one for the spectrum weighted with a gain in dB which increase linearly in frequency, and one with an equal and opposite linear decrease in frequency. In broad terms, this makes the estimate more reliant on the location of the band *edges* of the backscattered spectrum, rather than the values at the mid-band. Such an estimate is also shown in Figure 3 — the standard deviation of the signals is 0.55MHz for the phase zero and centroid estimates, but only 0.44MHz for the average weighted centroid estimate.

3.2 Reducing fluctuations in the attenuation estimate

We have already noted that there is a much larger variation in either the centre frequency or spectral division based methods for estimating attenuation than the quantity being measured. We therefore need some very strong prior information in order to extract the real attenuation value from the apparent value due to the statistical variation of backscatter. However, since we are measuring *cumulative* attenuation, we can make the assumption that this must increase monotonically with depth. This is always true when using eq. (23), but only the case for eq. (14) and eq. (19) if we

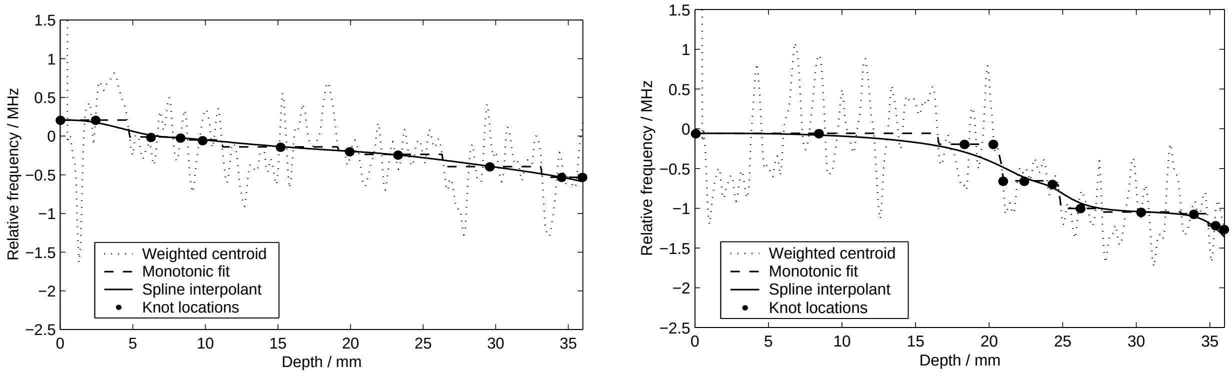

(a) Calibration phantom (b) Olive phantom

Figure 4: **Monotonic smoothing of frequency estimates.** The frequency centroid estimate (shown dotted) is first smoothed by calculating the best monotonic data fit (dashed). This controls the knot locations from which a cubic B-spline is interpolated. Knots are placed at the centre of each horizontal line, and at the ends of each discontinuity if it is a significant proportion of the bandwidth. (a) Shows results for a uniform attenuating phantom, and (b) for an attenuating olive embedded in low-attenuation jelly.

assume that z is everywhere similar to the value in the calibration phantom z_p.

A least-squares best fit monotonic function $y(t)$ can be found for noisy data $x(t)$ by using the *up-and-down blocks* or *pool adjacent violators* algorithm of Kruskal (1964). This is a very efficient algorithm (tending to $0(n^2)$ for n values, but in nearly all realistic cases much closer to $O(n)$) based on the observation that groups of data values which are not monotonic in the correct sense are most optimally replaced by a simple average. The implementation used here is not the same as the conventional one of Barlow et al. (1972), and is included in Appendix A.

One of the characteristics of this algorithm is that it tends to generate staircase like functions with large flat regions, especially where the input data has a large variance compared to the monotonic trend, as is the case here (see Figure 4). However, we expect the cumulative attenuation to be smooth as well as monotonically increasing (hence the frequency should be reducing). We can construct a smooth monotonic estimate by fitting an approximating spline to the monotonic function, where the flat 'steps' determine the location and number of knots; a similar concept was used by Hildenbrand and Hildenbrand (1986). In effect, the size of each step gives an indication of how well the original data fitted the monotonic model, and hence how closely we can justify the spline approximation fitting the data.

Here we place one knot in the centre of each step, and additional knots at the edges of steps if the subsequent drop is greater than a one quarter of the bandwidth of the probe. The approximation is achieved using cubic B-splines, which have the desirable property that they are continuous in both first and second derivatives. The solid lines in Figure 4 show the final results, with black circles indicating the knot locations in each case. The continuity of the spline leads to smoothing of both the cumulative attenuation α_e and the attenuation coefficient β_e.

Even with a careful definition of centre frequency, monotonic regression and spline approximation, the cumulative attenuation estimates still contain noise, which is evident when comparing those for

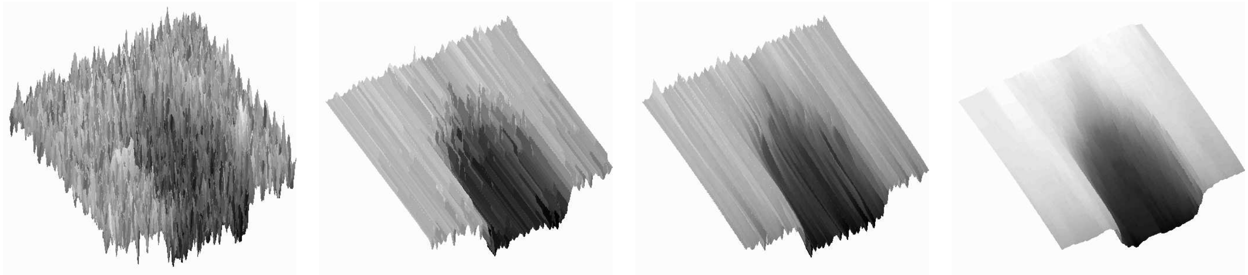

(a) (b) (c) (d)

Figure 5: **Reducing variation in the raw attenuation estimate.** (a) is the original estimate, (b) after monotonic regression, (c) after spline approximation in the axial direction and (d) after median filtering in the lateral direction.

each vector side by side, as in Figure 5(c). This lateral variation can be reduced by using a short range median filter in the lateral direction as a final step once α_e has been estimated for each vector independently. The end result is shown in Figure 5(d), and as a grey scale image in Figure 1(c).

4 Results

Two ultrasound phantoms were used to test the attenuation estimation algorithms. The first contained a homogeneous material with Rayleigh backscatter ($z = 4$ in eq. (2)) and a uniform attenuation of 0.4 dB/cm/MHz (J. M. Kofler and Madsen, 2001). This was also used for generating the calibration spectra. The second contained a stuffed olive embedded in raspberry jelly mixed with a concentration of flour. The jelly was set in two stages, with a different concentration of flour in each, such that the lower layer had greater backscatter than the higher. The olive had a greater attenuation than the surrounding jelly, which results in a shadow in the resulting ultrasound images, for instance the lower image of Fig. 1(a).

3D RF ultrasound data sets were acquired for each test object, using the real time RF acquisition system described in Appendix B. Ultrasound visualisations were generated using one of five methods:

BSCAN The conventional B-scan display of received amplitude.

SCATTER Attenuation correction using the method of Hughes and Duck (1997) which assumes that the attenuation is proportional to the backscatter.

CENTRE_FREQ Attenuation correction using eq. (14), with the average weighted centroid estimate of centre frequency.

SPEC_DIV Attenuation correction using spectral division by eq. (19).

SPEC_DIV_Z Attenuation correction using spectral division with estimation of backscatter power by eq. (23).

All of the CENTRE_FREQ, SPEC_DIV and SPEC_DIV_Z methods employed the monotonic and smoothness constraints outlined in Section 3. All methods have been implemented in Stradx software,

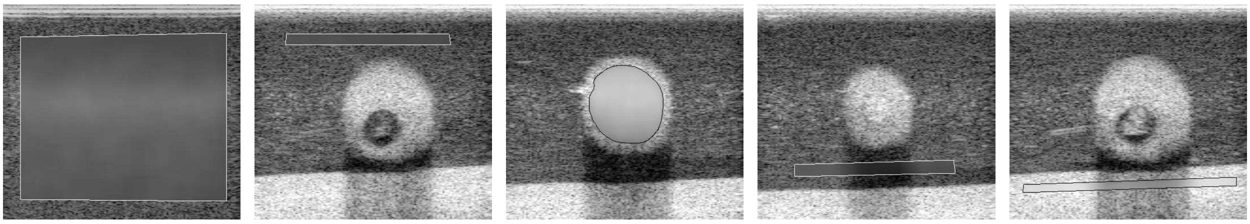

(a) (b) (c) (d) (e)

Figure 6: **Volumes used for assessing homogeneity.** Backscatter data based on each attenuation estimation method were assessed by considering the variance of small volumes over which the sample was known to be homogeneous. (a) The calibration phantom was assumed to be entirely homogeneous. The olive phantom was split into four distinct regions: (b) the background above the olive, (c) the olive (excluding the centre), (d) the background below the olive and (e) the lower layer with greater backscatter. Within each volume, backscatter data was averaged over a small range to minimise the influence of speckle, then the variance of this average calculated over the entire volume. Typical averaged data for one slice through each volume is shown within the outlined region in each figure.

and run in real time, at about 4-5 frames per second on a 3 GHz Pentium 4 CPU. The Fourier Transforms were implemented using the FFTW library[5] of Frigo and Johnson (1998).

The efficacy of each method was assessed by calculating the variation of gain over a large scale in volumes of 3D data known to be of a homogeneous material, as demonstrated in Figure 6. The gain variation over a small scale is due to speckle and was removed by appropriate averaging of the data. If attenuation estimation is successful, the display of homogeneous materials should itself be homogeneous. In addition, the attenuation estimate should not *add* significant variation to the corrected images.

4.1 Calibration phantom

Attenuation correction in the calibration phantom should be ideal for all methods, since there is no change in backscatter power between calibration spectra and the scan, and the scatter and attenuation are constant across the sample. The top row of Figure 7 shows that all methods produce images which are more homogeneous than BSCAN. Nevertheless, the noise in the attenuation estimation procedures adds variance to the images, and this is essentially what is measured for the non-BSCAN cases in Table 1.

Clearly, the SCATTER method exhibits the lowest noise levels, followed by CENTRE_FREQ and SPEC_DIV, then SPEC_DIV_Z. This is as expected from the analysis in Section 2 — for a homogeneous sample, SCATTER is simply an estimate of the slope of the gain with depth, which is very stable. CENTRE_FREQ and SPEC_DIV both involve essentially simple estimates of frequency. SPEC_DIV_Z requires estimation of an additional parameter, and hence introduces more noise. However, *all* images are visually acceptable, and have lower variance than the original BSCAN.

[5] http://www.fftw.org

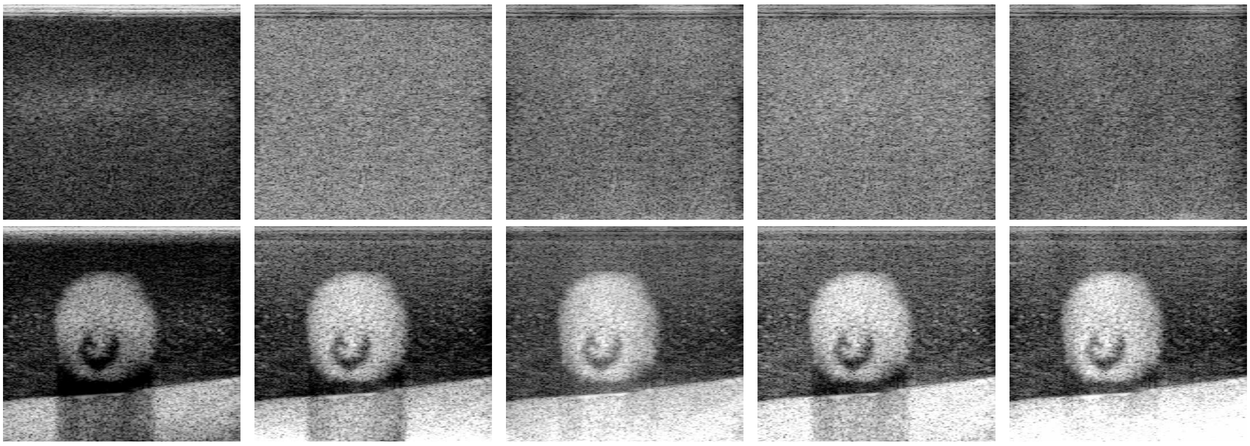

(a) (b) (c) (d) (e)

Figure 7: **Backscatter with varying methods of attenuation estimation.** The top row shows data from the calibration phantom, the bottom row from the olive phantom. (a) Shows a conventional BSCAN of the olive phantom. (b) to (e) show backscatter images with different attenuation estimation methods: (b) SCATTER, (c) CENTRE_FREQ, (d) SPEC_DIV and (e) SPEC_DIV_Z. (c) to (e) all employ the same monotonicity and smoothness constraints.

Table 1: **Homogeneity of backscatter for each attenuation estimate.** The table shows the standard deviation of the brightness of the local average backscatter values for each volume and each method. The units are arbitrary but comparable, since the overall gain was held constant over the measurements such that all backscatter values fell within the displayable brightness range.

			Attenuation estimate		
	BSCAN	**SCATTER**	**CENTRE_FREQ**	**SPEC_DIV**	**SPEC_DIV_Z**
Calibration phantom (Fig. 6(a))	11.47	3.33	5.52	5.54	8.06
Above olive (Fig. 6(b))	4.45	5.09	8.79	5.33	11.56
Olive (Fig. 6(c))	17.91	11.00	15.58	14.56	16.85
Below olive (Fig. 6(d))	20.89	10.47	7.80	14.94	8.44
Lower layer (Fig. 6(e))	33.36	18.61	9.01	21.29	12.05

4.2 Olive phantom

The olive phantom is a better test of the system, since it has different, and less well constrained, properties than the calibration object. Four test volumes were chosen in each case, shown in Figure 6(b) to (e), to test different properties of each method. Volume (b) is already homogeneous in BSCAN, and hence highlights noise in the other methods. The olive, volume (c), has a slight gain variation, which is not significant but should ideally be correctable. The other regions below the olive, (d) and (e), exhibit strong shadows which it is our specific aim to correct. The location of the four regions above each other also allows assessment of how independently each can be corrected. This is particularly important given the considerable smoothing required to reduce the variation in the attenuation estimates.

As with the calibration phantom, SCATTER exhibits the lowest variance in regions where the inherent assumptions are valid, e.g. above the olive and in the olive itself. However, the correction is poor in the lower regions, which still show strong shadows. SPEC_DIV has a similar performance, doing well in regions where BSCAN was already fairly homogeneous, but less well elsewhere. It is notable that SPEC_DIV is always worse than SCATTER, despite the latter apparently being reliant on more (potentially incorrect) assumptions.

The SPEC_DIV_Z method performs much better than SPEC_DIV in regions with strong shadowing, since it can account for variations in scatterer type. However, it is a more noisy estimate, and this noise degrades the performance in the other regions.

The CENTRE_FREQ method performs remarkably well in all circumstances; it has relatively low noise, but is not as biased as SCATTER or SPEC_DIV. This is the result of the analysis noted earlier that, although eq. (15) is the same as eq. (22) in the limit, the simplification is significantly less valid in the former case. In practice the additional terms in eq. (15) are important, and tend to improve the CENTRE_FREQ estimate. Visually, SPEC_DIV_Z appears to have the lowest bias, but the lower measurement noise in CENTRE_FREQ results in a better performance.

4.3 3D visualisation of olive phantom

Figure 8 is a 3D visualisation of the olive phantom which demonstrates the difficulty which shadowing and enhancement causes in such data. The reslice parallel to the skin surface (shown as a horizontal plane in the figure) appears as a fluid filled loop in an otherwise homogeneous material. It is only when this is corrected that it becomes clear that the centre is a separate material (the olive) and there is actually no fluid at all.

Figure 9 demonstrates the additional ability to display images of attenuation coefficient, defined in eq. (28). Whilst these are undoubtedly very noisy, the olive shows up very clearly as having higher attenuation than the surrounding material.

Both these examples also demonstrate the robustness of the presented algorithm (CENTRE_FREQ in this case), in that the reslices are based on several hundred images, all processed independently. The homogeneity of the reslices is an indication of the consistency of the gain adjustment in each of the original images.

5 Conclusion

It has been shown that correction of shadowing and enhancement artefacts is possible in *in vitro* data, at near real time rates, using spectral methods of attenuation estimation. The monotonicity and smoothness constraints are sufficient to reduce the estimation noise in all techniques to a level which

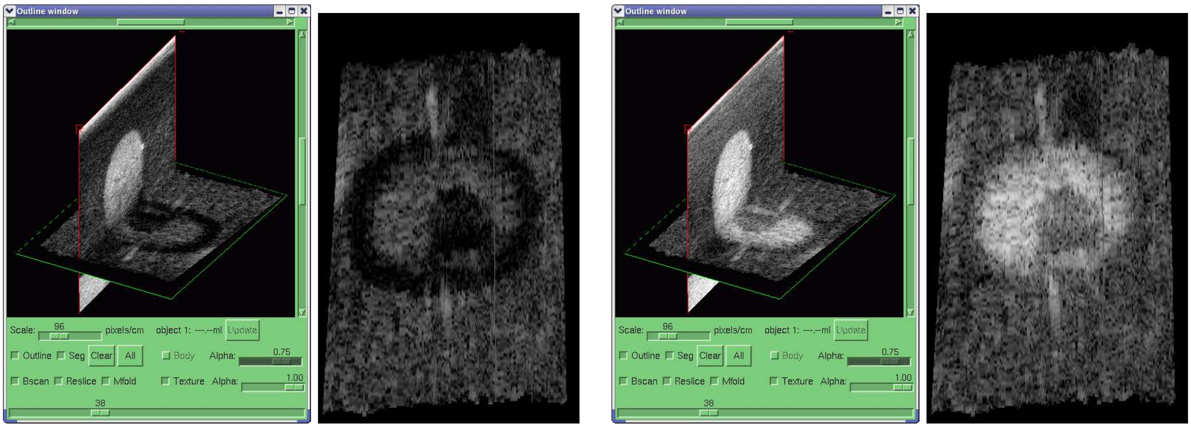

(a) BSCAN method

(b) CENTRE_FREQ method

Figure 8: **3D visualisations of olive phantom.** In each case one of the recorded frames of US data and an orthogonal reslice are shown in 3D on the left. On the right are the same reslice images, interpolated from all of the 150 recorded frames.

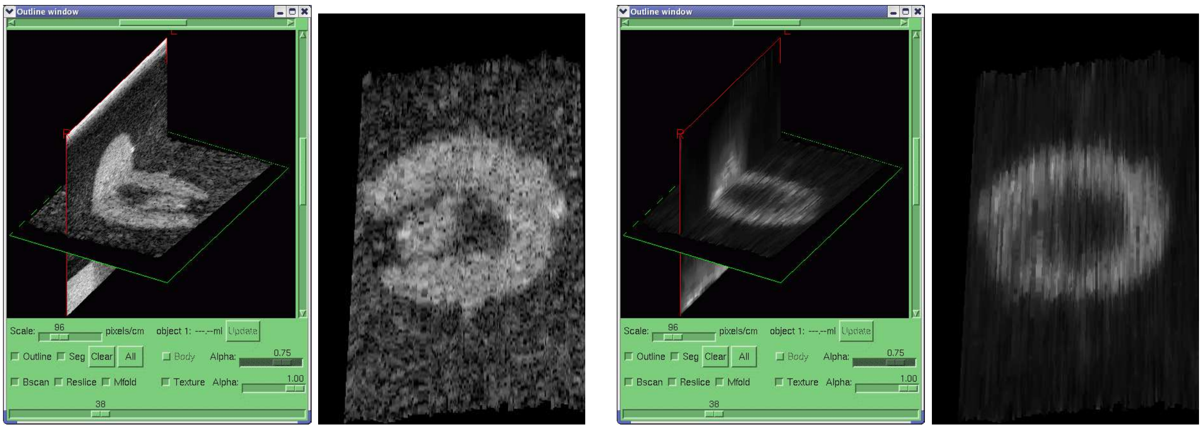

(a) Backscatter coefficient

(b) Attenuation coefficient

Figure 9: **Attenuation and backscatter of olive phantom.** The data is presented in the same format as in Figure 8.

results in acceptable visualisations after attenuation correction has been applied. This represents a significant step toward achieving accurate automatic gain correction on *in vivo* data.

The bias in each technique can be linked to sensitivity to scatterer type — this is demonstrated in both the *in vitro* results and the theoretical analysis. Using centre frequency currently represents the best trade-off between bias and measurement noise. The spectral division method with estimation of backscatter power shows promise as a low bias estimator, but requires more constraints to reduce the level of noise in the estimate.

The 3D RF system which we have set up will allow us to investigate the use of overlapping 3D RF data for imposing the additional constraints which are necessary to further reduce the noise in these measurements.

Acknowledgements

Graham Treece is supported by an EPSRC/RAEng Postdoctoral Fellowship. Dynamic Imaging Ltd. provided a modified ultrasound machine to enable the acquisition of analogue RF and digital amplitude ultrasound data in real time. Thanks also to Joel Lindop for making the olive phantom.

References

Baldeweck, T., Laugier, P., Herment, A., Berger, G., Jan. 1995. Application of autoregressive spectral analysis for ultrasound attenuation estimation: interest in highly attenuating medium. IEEE Transactions on Ultrasonics, Ferroelectrics, and Frequency Control 42 (1), 99–109.

Barlow, R. E., Bartholomew, R. J., Bremner, J. M., Brunk, H. D., 1972. Statistical inference under order restrictions. Wiley, New York.

Bevan, P. D., Sherar, M. D., 2001. B-scan ultrasound imaging of thermal coagulation in bovine liver: frequency shift attenuation mapping. Ultrasound in Medicine and Biology 27 (6), 809–817.

Bridal, S. L., Beyssen, B., Fornes, P., Julia, P., Berger, G., 2000. Multiparametric attenuation and backscatter images for characterization of carotid plaque. Ultrasonic Imaging 22 (1), 20–34.

Chen, Q., Zagzebski, J., Wilson, T., Stiles, T., 2002. Pressure-dependent attenuation in ultrasound contrast agents. Ultrasound in Medicine and Biology 28 (8), 1041–1051.

Damilakis, J., Stratakis, J., Perisinakis, K., Gourtsoyiannis, N., 2002. Broadband ultrasound attenuation imaging: algorithm development and clinical assessment of a region growing technique. Physics in Medicine and Biology 47 (2), 315–325.

Drukker, K., Giger, M. L., Mendelson, E. B., Jul. 2003. Computerized analysis of shadowing on breast ultrasound for improved lesion detection. Medical Physics 30 (7), 1833–1842.

Fink, M., Hottier, F., Cardoso, J. F., 1983. Ultrasonic signal processing for in vivo attenuation measurement: short time fourier analysis. Ultrasonic Imaging 5 (2), 117–135.

Flax, S. W., Pelc, N. J., Glover, G. H., Gutmann, F. D., McLachlan, M., 1983. Spectral characterization and attenuation measurements in ultrasound. Ultrasonic Imaging 5 (2), 95–116.

Frigo, M., Johnson, S. G., 1998. FFTW: An adaptive software architecture for the FFT. In: Proc. 1998 IEEE Intl. Conf. Acoustics Speech and Signal Processing. Vol. 3. IEEE, pp. 1381–1384.

Girault, J.-M., Ossant, F., Ouahabi, A., Kouamé, D., Patat, F., May 1998. Time-varying autoregressive spectral estimation for ultrasound attenuation in tissue characterization. IEEE Transactions on Ultrasonics, Ferroelectrics, and Frequency Control 45 (3), 650–659.

Gorce, J.-M., Friboulet, D., Dydenko, I., D'hooge, J., Bijnens, B. H., Magnin, I. E., Dec. 2002. Processing radio frequency ultrasound images: a robust method for local spectral features estimation by a spatially constrained parametric approach. IEEE Transactions on Ultrasonics, Ferroelectrics and Frequency Control 49 (12), 1704–1719.

Hildenbrand, K., Hildenbrand, W., 1986. On the mean income effect: data analysis of the U.K. family expenditure survey. In: Hildenbrand, W., Mas-Colell, A. (Eds.), Contributions to mathematical economics. North Holland.

Hughes, D. I., Duck, F. A., 1997. Automatic attenuation compensation for ultrasonic imaging. Ultrasound in Medicine and Biology 23 (5), 651–664.

J. M. Kofler, J., Madsen, E. L., 2001. Improved method for determining resolution zones in ultrasound phantoms with spherical simulated lesions. Ultrasound in Medicine and Biology 27 (12), 1667–1676.

Jensen, J. A., 1996. Field: A program for simulating ultrasound systems. Medical and Biological Engineering and Computing 34, Supp. 1 (1), 351–353.

Knipp, B. S., Zagzebski, J. A., Wilson, T. A., Dong, F., Madsen, E. L., 1997. Attenuation and backscatter estimation using video signal analysis applied to B-mode images. Ultrasonic Imaging 19 (3), 221–233.

Kruskal, J. B., 1964. Nonmetric multidimensional scaling: a numerical method. Psychometrika 29, 115–129.

Lu, Z. F., Zagzebski, J. A., Madsen, E. L., Dong, F., 1995. A method for estimating an overlying layer correction in quantitative ultrasound imaging. Ultrasonic Imaging 17 (4), 269–290.

Nicholas, D., Hill, C. R., Nassiri, D. K., 1982. Evaluation of backscattering coefficients for excised human tissues: principles and techniques. Ultrasound in Medicine and Biology 7, 7–16.

O'Donnel, M., H. F. Reilly, J., May 1985. Clinical evaluation of the B/-Scan. IEEE Transactions on Sonics and Ultrasonics SU-32 (3), 450–457.

Pesavento, A., Lorenz, A., Siebers, S., Emmert, H., 2000. New real-time strain imaging concepts using diagnostic ultrasound. Physics in Medicine and Biology 45 (6), 1423–1435.

Pesavento, A., Perrey, C., Krueger, M., Ermert, H., Sep. 1999. A time-efficient and accurate strain estimation concept for ultrasonic elastography using iterative phase zero estimation. IEEE Transactions on Ultrasonics, Ferroelectrics and Frequency Control 46 (5), 1057–1067.

Prager, R. W., Gee, A. H., Berman, L., 1999. Stradx: real-time acquisition and visualisation of freehand 3D ultrasound. Medical Image Analysis 3 (2), 129–140.

Prager, R. W., Gee, A. H., Treece, G. M., Berman, L., 2003. Decompression and speckle detection for ultrasound images using a homodyned k-distribution. Pattern Recognition Letters 24 (4–5), 705–713.

Taxt, T., Jul. 2001. Three-dimensional blind deconvolution of ultrasound images. IEEE Transactions on Ultrasonics, Ferroelectrics, and Frequency Control 48 (4), 867–871.

Treece, G. M., Gee, A. H., Prager, R. W., Cash, C. J. C., Berman, L. H., Apr. 2003. High definition freehand 3D ultrasound. Ultrasound in Medicine and Biology 29 (4), 529–546.

Tu, H., Varghese, T., Madsen, E. L., Chen, Q., Zagzebski, J. A., 2003. Ultrasound attenuation imaging using compound acquisition and processing. Ultrasonic Imaging 25 (4), 245–261.

Tyréus, P. D., Diederich, C., 2004. Two-dimensional acoustic attenuation mapping of high-temperature interstitial ultrasound lesions. Physics in Medicine and Biology 49 (4), 533–546.

Valckx, F. M. J., Thijssen, J. M., van Geemen, A. J., Rotteveel, J. J., Mullaart, R., 2000. Calibrated parametric medical ultrasound imaging. Ultrasonic Imaging 22 (2), 57–72.

Walach, E., Shmulewitz, A., Itzchak, Y., Heyman, Z., Feb. 1989. Local tissue attenuation images based on pulsed-echo ultrasound scans. IEEE Transactions on Biomedical Engineering 36 (2), 211–221.

Watson, R. J., McLean, C. C., Moore, M. P., Spencer, T., Salter, D. M., Anderson, T., Fox, K. A. A., McDicken, W. N., 2000. Classification of arterial plaque by spectral analysis of in vitro radio frequency intravascular ultrasound data. Ultrasound in Medicine and Biology 26 (1), 73–80.

Xiao, G., Brady, J. M., Noble, J. A., Apr. 2002. Nonrigid registration of 3-D free-hand ultrasound images of the breast. IEEE Transactions on Medical Imaging 21 (4), 405–412.

Appendices

A Monotonic regression

The following is a memory and time efficient implementation of the up-and-down blocks algorithm by Kruskal (1964) for regression of a piecewise linear monotonic function y to data x:

```
/* return a length n output vector y which is the best monotonic fit to x
   if (sense = 1), y will be monotonically increasing
   if (sense = -1), y will be monotonically decreasing */
void monotonic_regression( int n; float *x, float *y, int sense )
{
  int i, j;                /* i is the current data length, j the range of the current mean */
  float sum;                                        /* the current sum over the range j */

  sum = x[0]; j = 1;                                         /* initialise sum and range j */
  for (i=1; i<n; i++) {         /* add one value at a time, enforcing monotonicity from 0..i */
    if ( (x[i] - sum/j)*sense < 0 ) {                /* is x[i] consistent with the current mean? */
      sum += x[i]; j++;                        /* NO - extend range j of mean forward by one */
      while ( (j<=i) && ((y[i-j] - sum/j)*sense > 0) ) { /* is the mean consistent with y[i-j]? */
        sum += x[i-j]; j++;                       /* NO - extend range j of mean back until it is */
      }
```

```
    } else {                                /* YES - no need to extend range j of mean */
      sum /= j;                                              /* calculate mean value */
      for (; j>0; j--) y[i-j] = sum;                        /* set y to mean from i-j..i-1 */
      sum = x[i]; j = 1;                                /* re-initialise sum and range j */
    }
  }
  sum /= j;                                                  /* calculate mean value */
  for (; j>0; j--) y[i-j] = sum;                            /* set y to mean from i-j..n-1 */
}
```

B Real time RF acquisition system

Attenuation estimation using the methods outlined in Section 2 relies on the ability to acquire RF ultrasound data. This needs to be high resolution, since the RF data is acquired before log-compression, and so that adjustments in gain after acquisition do not simply amplify noise in the signal. Ideally we would like to be able to acquire 3D RF data, since one of the aims of shadowing and enhancement correction is to make visualisations from 3D data easier to interpret.

Ultrasound RF analysis reported in the literature is often based on single frames acquired at only 8-bit sampling resolution, with several minutes delay to download the data to an external PC (Watson et al., 2000). A 3D RF system using 16-bit acquisition at 20MHz has been reported (Taxt, 2001), but not in real-time. Similarly a real-time system using 12-bit acquisition at 30 MHz has been reported (Pesavento et al., 2000), but not in 3D. Commercial RF systems have until recently been neither real-time nor 3D. The system we have developed, Stradx[6] (Prager et al., 1999), is based on the freehand scanning protocol, where the probe is moved by hand whilst being tracked by an external position sensor. RF ultrasound frames and their respective positions are temporally matched, and the resulting 3D data stored in real time. 2D backscatter images can be displayed in real time, and 3D visualisation and analysis can be performed immediately after acquisition. The non-RF version of this system has recently been shown to have a positional accuracy of ± 0.6 mm (Treece et al., 2003).

Analogue RF ultrasound signals are digitised after focusing and time-gain compensation, but before log-compression and envelope detection, using a Gage Compuscope CS14100[7] 14-bit digitiser. The required signals are shown in Figure 10: we use a Dynamic Imaging Diasus[8] ultrasound machine. Whole frames are stored in on-board Gage memory, before transferring to PC memory at 75 Mb/s. On average 30-60 frames can be acquired per second.

RF phase and amplitude precision were assessed by scanning a planar target at 2cm depth, in a water bath, with a 5-10MHz probe. 100 frames of data were recorded, keeping the probe and target still, using 50 and 100 MHz asynchronous, and 66 MHz synchronous sampling rates. Typical magnitude and phase images are shown in Figure 11(a) and (b): the rectangle in each case indicates the area within which data was analysed. Figure 11(c) shows a clear improvement in inter-vector precision when using synchronous acquisition.

Intra-vector signal variation also showed a dramatic improvement using synchronous acquisition. The standard deviation was $\pm 0.2°$ phase, ± 1.7 bits amplitude (66 MHz synchronous), compared to $\pm 6.4°$, ± 4.2 bits (100 MHz asynchronous) and $\pm 13.2°$, ± 5.5 bits (50 MHz asynchronous). The

[6] http://mi.eng.cam.ac.uk/~rwp/stradx/
[7] http://www.gage-applied.com
[8] http://www.dynamicimaging.co.uk

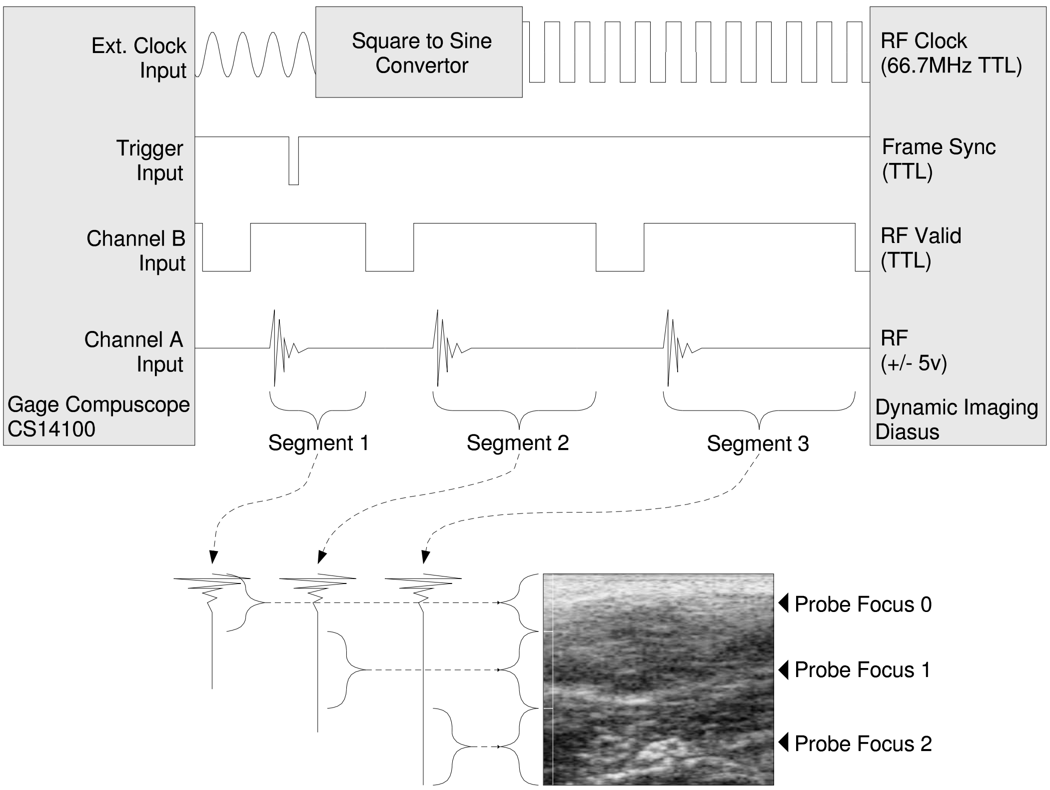

Figure 10: **Connections between the ultrasound machine and the PC.** Two signals are required in addition to the received RF ultrasound: one showing the frame start, and one the valid receive portion of the RF signal. If in addition the ultrasound clock is available, this can be used to synchronise the sampling, which greatly improves the repeatability. The diagram shows the general case of multiple transmit focii: in practice, only one transmit focus was used throughout this work.

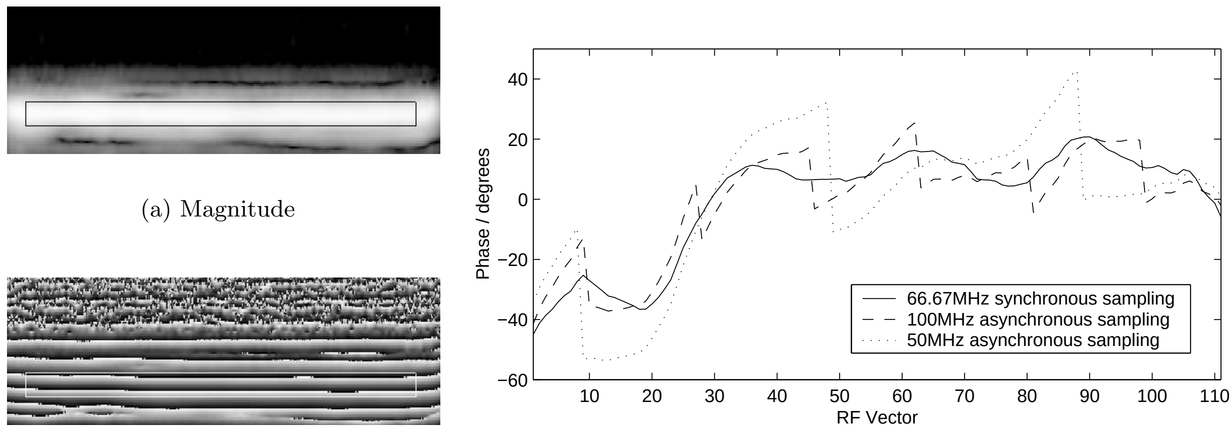

(a) Magnitude

(b) Phase

(c) Inter-vector phase variation

Figure 11: **The effect of sampling on inter-vector variation.** A flat surface was repeatedly scanned in a water bath: (a) shows the magnitude, and (b) the phase from a typical scan, zoomed x10 in the vertical direction. Magnitude and phase values where analysed within the rectangle shown in each image. (c) The typical phase variation across vectors for each sampling method. Some residual variation is expected since the surface will not be precisely smooth.

acquisition was notionally 14-bit, with an effective dynamic range of 11.7 bits, hence the magnitude variation for synchronous acquisition was within the noise floor of the analogue to digital converter.